

A comprehensive observational study of the FRB 121102 persistent radio source

GE CHEN,¹ VIKRAM RAVI,¹ AND GREGG W. HALLINAN¹

¹*Cahill Center for Astronomy and Astrophysics, MC 249-17 California Institute of Technology, Pasadena CA 91125, USA*

Submitted to

ABSTRACT

FRB 121102 is the first fast radio burst source to be spatially associated with a persistent radio source (QRS121102), the nature of which remains unknown. Motivated by the importance of the potential insights into the origins of FRBs, we present a detailed observational study of QRS121102 and its host galaxy. We constrain the physical size of QRS121102 by measuring its flux-density variability with the VLA in the Ku-band (12 to 18 GHz) and the K-band (18 to 26 GHz). Any such variability would likely be due to Galactic refractive scintillation, and would require the source radius to be $\lesssim 10^{17}$ cm at the host-galaxy redshift. We found the radio variability to be lower than the scintillation theory predictions for such a small source, leaving open the possibility for non-AGN models for QRS121102. In addition, we roughly estimated the mass of any potential supermassive black hole (BH) associated with QRS121102 from the width of the H α emission line using a medium-resolution optical spectrum from the Keck Observatory. The line width gives a velocity dispersion of $\lesssim 30$ km/s, indicating a supermassive BH mass of $\lesssim 10^{4\sim 5} M_{\odot}$. We find the supermassive BH mass too low for the observed radio luminosity, and X-ray luminosity constraints, if QRS121102 were an AGN. Finally, some dwarf galaxies that host supermassive black holes may be the stripped cores of massive galaxies during the tidal interactions with companion systems. We find no nearby galaxy at the same redshift as the QRS121102 host from low-resolution Keck spectra, or from the PanSTARRS catalog. In conclusion, we find no evidence supporting the hypothesis that the persistent radio source associated with FRB 121102 is an AGN. We instead argue that the inferred size, and the flat radio spectrum, favors a plerion interpretation. We urge continued broadband radio monitoring of QRS121102 to search for long-term evolution, and the detailed evaluation of potential analogs that may provide greater insight into the nature of this remarkable, mysterious class of object.

Keywords: High energy astrophysics: Radio bursts — Transient sources: Radio transient sources—
Stellar astronomy: Neutron stars

1. INTRODUCTION

Fast radio bursts (FRBs) are a class of transient phenomena wherein energies $\gtrsim 10^{35}$ erg are released on timescales $\ll 1$ s at radio wavelengths (e.g. Lorimer et al. 2007). The progenitor and emission processes of FRBs remain uncertain. Hundreds of FRB sources have been reported, and over 20 of them have been found to repeat (e.g. The CHIME/FRB Collaboration et al. 2021). Repeaters and non-repeaters are reported to show statistically different characters (luminosity, pulse

width, temporal-spectral structures, etc.), yet it remains unclear whether or not they originate from two distinct populations. FRB 121102 was the first repeater detected (Spitler et al. 2016; Scholz et al. 2016), and so far one of the most extensively studied FRB sources. The bursts are found to have a ~ 160 -day periodicity (Cruces et al. 2021), and the source has been localized within a star forming region of a low-metallicity dwarf galaxy at a redshift of 0.19273 (Bassa et al. 2017; Marcote et al. 2017; Tendulkar et al. 2017), giving a luminosity distance of 971 Mpc (using the recent Planck results implemented in *astropy*: $H_0 = 67.4$ km s⁻¹ kpc⁻¹, $\Omega_m = 0.315$, $\Omega_{\Lambda} = 0.685$; Planck Collaboration et al. 2020).

FRB 121102 is one of only two FRBs reported to be spatially associated with persistent radio emission of unknown origin (Tendulkar et al. 2017; Niu et al. 2021). In the case of FRB 121102, the centroid of the persistent emission is within 12 mas (40 pc; 95% confidence level) from the FRB source. The emission shows a flat spectrum from ~ 400 MHz to ~ 6 GHz (flux density $\approx 200 \mu\text{Jy}$), and decreases at higher frequencies (166 ± 9 , 103 ± 7 and $66 \pm 7 \mu\text{Jy}$ at 10, 15 and 22 GHz, respectively) (Chatterjee et al. 2017; Resmi et al. 2020). It remains unresolved by very long baseline interferometry (VLBI) at 5 GHz, indicating a radius below ~ 0.2 mas, or $\sim 10^{18}$ cm (0.35 pc) at the host-galaxy redshift (Tendulkar et al. 2017). A flux-density amplitude modulation of $\sim 30\%$ has been reported at 3 GHz (Chatterjee et al. 2017), consistent with refractive scintillation by the Milky Way interstellar medium (ISM) (e.g., Romani et al. 1986; Walker 1998). No X-ray counterpart has been detected with XMM-Newton and Chandra (Chatterjee et al. 2017).

If we remain agnostic regarding models for the origin of FRBs, a compact radio source like that associated with FRB 121102, with a luminosity of $\sim 2 \times 10^{29} \text{ erg s}^{-1} \text{ Hz}^{-1}$, would most likely be ascribed to AGN activity. Several AGN-like radio sources of similar luminosities have been reported to be hosted by dwarf galaxies (e.g. Reines et al. 2020; Mezcua et al. 2019). Although Tendulkar et al. (2017) has found the host-galaxy optical spectrum to be consistent with intense star formation based on the BPT diagnostics (Baldwin et al. 1981), it is rare but not unheard of (at the $\sim 0.1\%$ level; Sabater et al. 2019) for galaxies classified as star forming according to BPT diagnostics to host radio-loud AGN. This may be substantially more common among the dwarf galaxy population: the majority of the Reines et al. (2020) sample of dwarf galaxies with optical spectra hosting candidate radio AGN are classified as star forming on BPT diagrams. The radio source associated with FRB 121102 is too compact and too luminous to be associated with star-formation activity (Chatterjee et al. 2017). Other possible origins include a supernova afterglow powered by interaction with a dense circum-stellar medium (Dong et al. 2021), the afterglow of a long-duration gamma-ray burst (e.g., Berger et al. 2003), and an extreme pulsar wind nebula (PWN; e.g., Margalit & Metzger 2018).

In this paper, we investigate the nature of the persistent radio source associated with FRB 121102 (“QRS121102” hereafter) using new data from the Karl G. Jansky Very Large Array (VLA) and the Low Resolution Imaging Spectrometer (LRIS) at the Keck Observatory. We adopt the host redshift of 0.19273 (Ten-

dulkar et al. 2017) for all relevant calculations hereafter. In Section 2, we describe the observations. In Section 3, we first measure the flux-density modulation of QRS121102 in the K-band (18 to 26 GHz) and the Ku-band (12 to 18 GHz), where refractive scintillation is expected to produce larger modulations than previously observed at 5 GHz. We also separately investigate the hypothesis that QRS121102 is powered by a supermassive or intermediate-mass black hole (BH) using a medium-resolution LRIS spectrum, and evaluate whether or not the host galaxy belongs to a galaxy group using the low-resolution LRIS spectra. In Section 4, we first constrain the size of QRS121102 by comparing its flux-density modulation with that predicted by scattering theory. In addition, we compare the AGN population with our dynamical BH mass estimation, stellar mass estimation, and radio and X-ray luminosity constraints. We conclude in Section 5 that an AGN hypothesis for QRS121102 is unlikely.

2. OBSERVATIONS

2.1. VLA radio observations

We have observed the persistent radio source (QRS121102) in the VLA K-band (18 to 26 GHz) and Ku-band (12 to 18 GHz) using the C configuration. The channel width was 2 MHz and the integration time was 3 s for the K-band observations and 2 s for the Ku-band observations. The observations include six epochs from 2017 May 29 to 2017 August 10 (Table 1). In each epoch, the observation started with a single scan of the primary calibrator 3C147 (Field 0) for flux scale and bandpass calibration, and then a few cycles of the phase calibrator 1 J0555+3948 (Field 1), phase calibrator 2 J0518+3306 (Field 2), and QRS121102 (Field 3) (Table 2).

2.2. Keck optical observations

The optical spectra used in this work were obtained using Keck/LRIS. We obtained two types of observations. One, with medium spectral resolution, was used to measure the spectral width of the $\text{H}\alpha$ emission line associated with the FRB 121102 host galaxy. The other, with low spectral resolution, used two slit orientations to obtain spectra of galaxies immediately adjacent to the FRB 121102 host.

The medium resolution spectrum of the FRB 121102 host was obtained on October 12, 2018 using the 1.0” longslit and the D560 dichroic. The red side used the grating with 1200 lines/mm blazed at 7500 Å and targeted the $\text{H}\alpha$ emission.

Low resolution spectra of the host and nearby sources were obtained on 2017 January 26 using the 1.5” long slit and the 560 dichroic. The grating used on the red

Table 1. VLA Observations and Results

Obs.	Epoch (YYYY-MM-DD hh:mm)	Band	3C147 (f0) (Jy)	J0555+3948 (f1) (mJy)	J0518+3306 (f2) (mJy)	QRS121102 (f3) (μ Jy)
1	2017-05-29 16:09	K	1.994 ± 0.010	1956.5 ± 2.5	153.1 ± 5.3	56.6 ± 8.2
2	2017-06-03 16:43	K	2.010 ± 0.013	2135.8 ± 3.4	143.9 ± 2.5	52.4 ± 7.0
3	2017-06-08 08:19	U	2.82 ± 0.11	2242 ± 15	200.2 ± 1.7	67 ± 13
4	2017-06-10 21:25	U	2.857 ± 0.010	2565 ± 30	214.5 ± 5.7	118.0 ± 5.5
5	2017-06-11 16:32	U	2.799 ± 0.018	2431.2 ± 6.4	158.2 ± 2.5	82.1 ± 6.4
6	2017-08-10 12:31	K	2.050 ± 0.026	2148.4 ± 7.5	193.6 ± 5.4	109 ± 14
	2017-08-10 06:04	U	2.804 ± 0.026	2217.7 ± 6.0	144.0 ± 4.3	63.5 ± 6.3

Table 2. VLA Targets

Field	Target	RA	DEC	Intention	Single Scan Duration (Minutes)
0	J0542+4951 (3C147)	$05^{\text{h}}42^{\text{m}}36.1^{\text{s}}$	$+49^{\circ}51'07.2''$	Flux and Bandpass Calibrator	6
1	J0555+3948	$05^{\text{h}}55^{\text{m}}30.8^{\text{s}}$	$+39^{\circ}48'49.2''$	Phase Calibrator 1 ^a	1.5
2	J0518+3306	$05^{\text{h}}18^{\text{m}}05.1^{\text{s}}$	$+33^{\circ}06'13.4''$	Phase Calibrator 2 ^b	1.5
3	QRS121102	$05^{\text{h}}31^{\text{m}}58.7^{\text{s}}$	$+33^{\circ}08'52.5''$	Science	10

^aUsed as the phase calibrator during our CASA imaging process.

^bTreated as a science target during our CASA imaging process.

Table 3. Summary of Optical Observations

Date (YYYY-MM-DD)	Instrument	Grating, Grism (Red, Blue)	λ (Red, Blue; Å)	Slit	Resolution (1σ) (Å)	Exposure (Minutes)
2018-10-12	LRIS	1200/7500, 400/3400	NA	long 1.0"	~ 1	80 ^a
2017-01-26	LRIS	400/8500, 600/4000	5462 \sim 10318, 3122 \sim 5603	long 1.5"	~ 4	50

^aEach exposure is 20 minutes. The total exposure time is 80 minutes when combining all four exposures, and 40 minutes after excluding the two exposures polluted by cosmic rays (see Section 3.2).

side has 400 lines / mm blazed at 8500 Å, covering wavelength from about 5462 Å to 10318 Å, with a dispersion of 1.86 Å/pixel. We estimate the spectral resolution to be ~ 4 Å (1σ) from the weighted average width of the four isolated skylines (5577.0 Å, 5898.0 Å, 6315.7 Å, 7257.4 Å). On the blue side the grism has 600 lines / mm blazed at 4000 Å, covering wavelengths from 3122 Å to 5603 Å. Standard stars were observed for the flux response calibration, arc-lamp spectra were obtained for the wavelength calibration, and bias frames were taken

for the bias-subtraction. The flat field was generated using dome flats.

3. DATA ANALYSIS AND RESULTS

3.1. VLA flux density measurements

In this section, we describe how we measure the radio flux density of QRS121102 in each epoch.

The visibility data were calibrated and imaged using CASA following the standard procedures (task names

shown in parentheses).¹ In the calibration, the VLA antenna positions were updated (*genical*). The primary calibrator 3C147 was used to find the absolute scale of the gain amplitudes by referring to the standard flux density (*setjy*), and to correct for the instrumental delay and the complex antenna-response variation with frequency (*bandpass*). The complex gain solutions (both amplitude and phase) were obtained from the phase calibrator 1, J0555+3948, that is $\sim 8^\circ$ apart from QRS121102 (CASA task *gaincal*), and the gain amplitudes were properly-scaled using the absolute scale just obtained using 3C147 (*fluxscale*). All calibration solutions were then applied (*applycal*) to QRS121102, as well as the fainter phase calibrator 2, J0518+3306 ($\sim 2^\circ$ away from QRS121102). After calibration, potential radio frequency interference (RFI) and internally generated signals were removed by flagging out narrow-banded spikes in the spectra (*flagdata*). In epoch 3, one scan of QRS121102 was removed as it was several times brighter than the others (within 30 minutes apart) due to strong RFI, or perhaps a passing cloud.

The calibrated visibility data were binned to 20 s and 500 kHz to speed up synthesis imaging using the CASA task (*split*). The data were gridded and Fourier transformed and the synthesized beam was deconvolved (*tclean*). The FWHM of the synthesized beam was $\sim 1.5''$ (major axis) $\times 1.2''$ (minor axis) in the Ku-band and $\sim 1.3''$ (major axis) $\times 0.9''$ (minor axis) in the K-band in C configuration. Our images were created using a small cell size of $0.1'' \times 0.1''$ and a Briggs robust weighting of 0.5 (Briggs 1995).

We measured the flux density of each source from the images by fitting each with a 2-D Gaussian model (*imfit*; Fig.1). We obtained the flux density of those point sources (based on the criterion implemented by the CASA *imfit* task) from the peak, and of the others from the integrated flux density within each fitting region. Uncertainties were calculated by propagation of errors of the 2D fitting model. Table 1 lists the results and Fig. 2 shows the flux density light curves in both bands.

The angular size of QRS121102 has been reported to be under ~ 0.2 mas at 5 GHz as measured by the Very-long-baseline interferometry (VLBI) (Marcote et al. 2017). It is expected to be unresolved in our observations, where the beam FWHM is $\sim 1.4''$ in the Ku-band and $\sim 0.9''$ in the K-band. In our images, the 2D Gaussian fitting results show that QRS121102 is a point

source in all but epoch 3, where the image is marginally resolved as 1.13 ± 0.61 arcsec along the major axis and 0.49 ± 0.22 arcsec along the minor axis (FWHM, deconvolved from beam). This is likely due to the remaining phase errors in the calibration solution, as the image of phase calibrator 2 J0518+3306 appears highly distorted. The errors were removed by phase-only self-calibration in field 2, but not in field 3, for reasons outlined below.

In field 3, our observations of QRS121102 were affected by a bright source, NVSS J053153+331014, that is $\approx 1.8'$ (twice of the primary beam FWHM in the Ku-band) away from the pointing center (QRS121102) and over one order-of-magnitude brighter (≈ 3 mJy in flux density before correcting for primary-beam attenuation). To reduce the associated errors, we performed self-calibration (phase only) for NVSS J053153+331014 and QRS121102 simultaneously. We also tried to remove the flux density contribution from NVSS J053153+331014 modeled from self-calibration, and then subtract the model visibility from the corrected visibility data. Neither attempt made a significant improvement on the image of QRS121102, since self-calibration failed to correct the beam model error far away from the pointing center.

In addition, there might be remaining calibration errors since the flux densities of the two phase calibrators, J0555+3948 and J0518+3306, also vary by $\sim 4\%$ and $\sim 10\%$ throughout the epochs in each band (Fig. 2). The variations are likely not intrinsic to the source for two reasons. (1) J0555+3948 has been reported to vary by 2.0% on a time scale of 251 days at 33 GHz and 3.4% on a time scale of 293 days at 16 GHz (Franzen et al. 2009). It is unlikely to show a greater variability on a timescale of days, as been observed in this work (e.g. epochs 3, 4, 5). (2) More importantly, the flux density light curve of QRS121102 shows a moderate positive correlation with that of J0555+3948, and a strong positive correlation with that of J0518+3306, with a correlation coefficient of 0.67 and 0.91, respectively. To reduce potential calibration errors, in each epoch we re-scaled the flux density measurements of QRS121102 by those of the two phase calibrators (Fig. 3). We adopt the flux density scaled by J0518+3306 (phase calibrator 2) thereafter, since it has a smaller angular separation from QRS121102.

3.2. Keck/LRIS Medium Resolution Spectral Analysis

The LRIS data were processed using the LRIS automated reduction pipeline (LPipe; Perley 2019) following standard procedures: subtract the bias, make flat fields and apply flat-field correction, remove cosmic ray pixels, model and remove sky lines, perform wavelength calibra-

¹ The Common Astronomy Software Applications (CASA) is a software package developed by the NRAO.

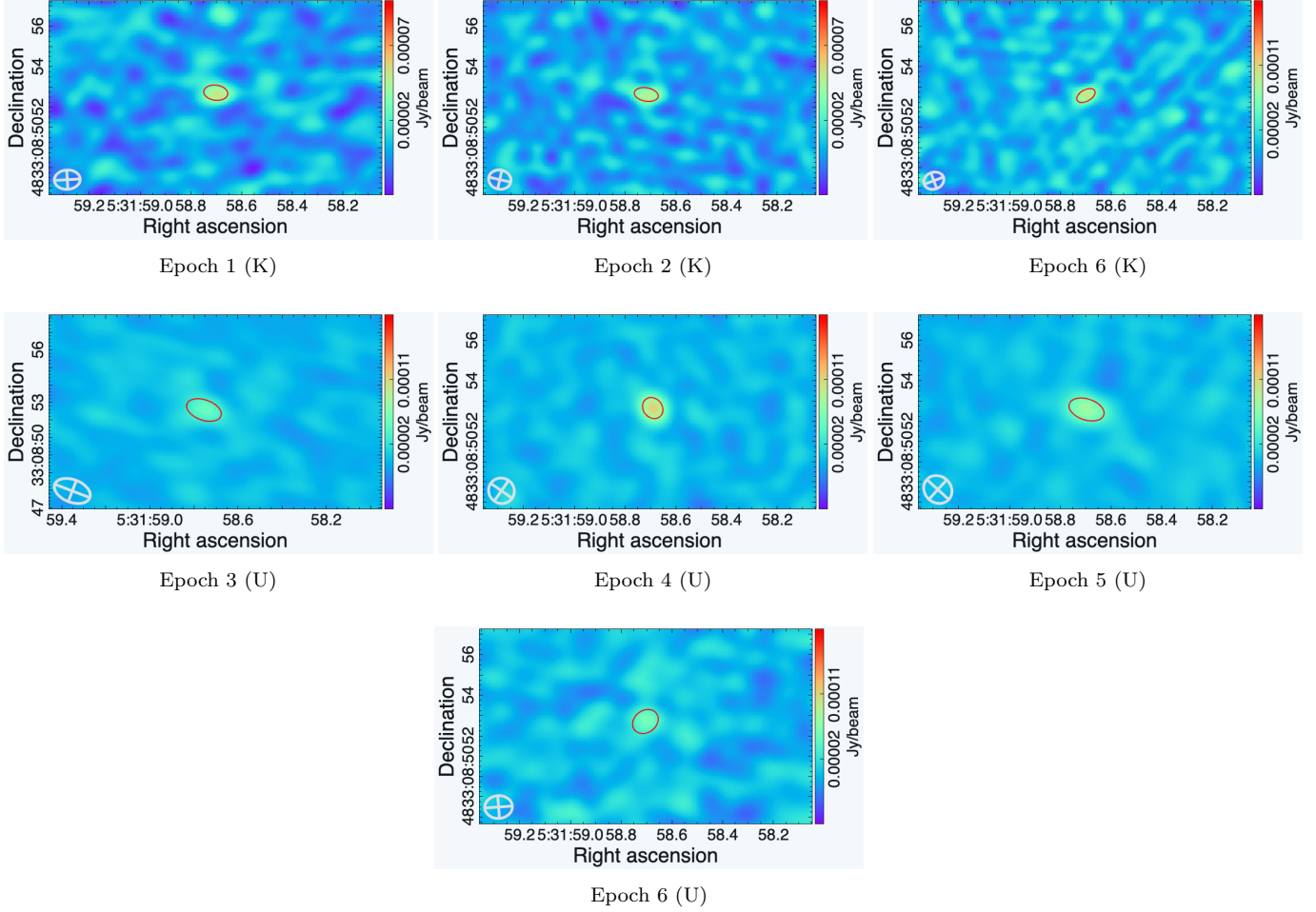


Figure 1. VLA images (in J2000 coordinates) of QRS121102 in seven epochs, with band indicated in parentheses. The color scale represents flux density in Jy / beam (see color bar). The open light gray circle (on the bottom left of each image) shows the synthesized beam size (1σ) and the red circle shows the 1σ 2D Gaussian fitting results convolved with the synthesized beam. The position angles of the best fit results are consistent with those of the clean beams within 1σ in all cases where the source is unresolvable.

tion by referring to the arc lamp spectra, and determine the flux response function by observing standard reference stars. The processed 2D spectrum targets the H α emission.

The width of the H α emission line is produced by multiple effects (Rybicki & Lightman 1979)–

- dynamical velocity dispersion due to gravity,
- instrumental broadening,
- random thermal motions,
- natural broadening,
- turbulent motions.

In this section, we test the hypothesis that QRS121102 is associated with an AGN by using the velocity dispersion

to roughly constrain the mass of a potential supermassive BH. The velocity dispersion is estimated from the H α line width.

The H α emission line width of the host is determined by fitting the rest-frame 2D spectrum with a 2D Gaussian function whose rotation angle is fixed at zero, plus a constant offset. We convert the observed 2D spectrum of the host into the rest-frame wavelength using a previously reported redshift of 0.19273 (Tendulkar et al. 2017). The width (1σ) of the emission line is $0.9316 \pm 0.0026 \text{ \AA}$ when combining all four exposures, and $0.8947 \pm 0.0015 \text{ \AA}$ after removing the two exposures polluted by the nearby cosmic rays (Fig. 4). A bright pixel at the center of the H α emission is seen in the residual (bottom panel of Fig. 4), but no extended structure that might impact the emission width result is found.

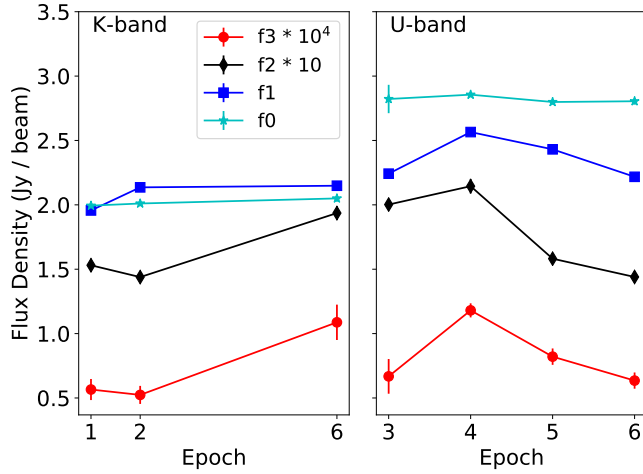


Figure 2. Flux density light curve of the K-band (left) and the Ku-band (right). f3, f2, f1 and f0 represents the flux density of QRS121102 (solid red circle), the phase calibrator 2 (solid black diamond), the phase calibrator 1 (solid blue square) and the prime calibrator (cyan stars), respectively. f3 and f2 are scaled by 10^4 and 10 times for display. Details of the observations are shown in Tables 1, 2.

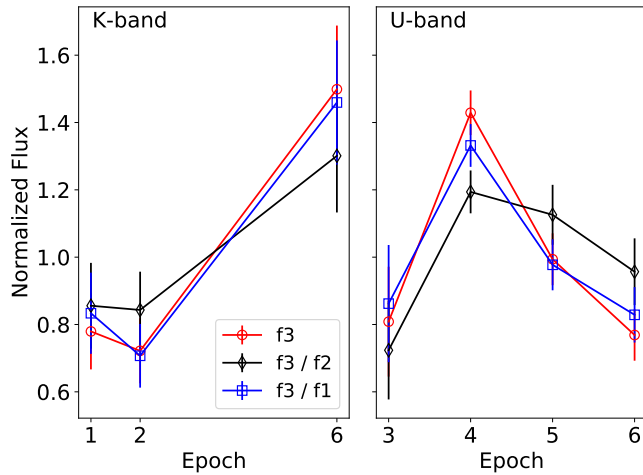


Figure 3. Normalized (and scaled) flux density light curve of the K-band (left) and the Ku-band (right). f3, f2 and f1 represents the flux density of QRS121102, the phase calibrator 2 and the phase calibrator 1, respectively. Red open circles (f3) show the normalized flux density of QRS121102, black open diamonds (f3/f2) show the flux density of QRS121102 divided by those of the phase calibrator 2 and then normalized to average at unity, and blue open squares (f3/f1) are the flux density of QRS121102 divided by those of the phase calibrator 1 and then normalized to average at unity.

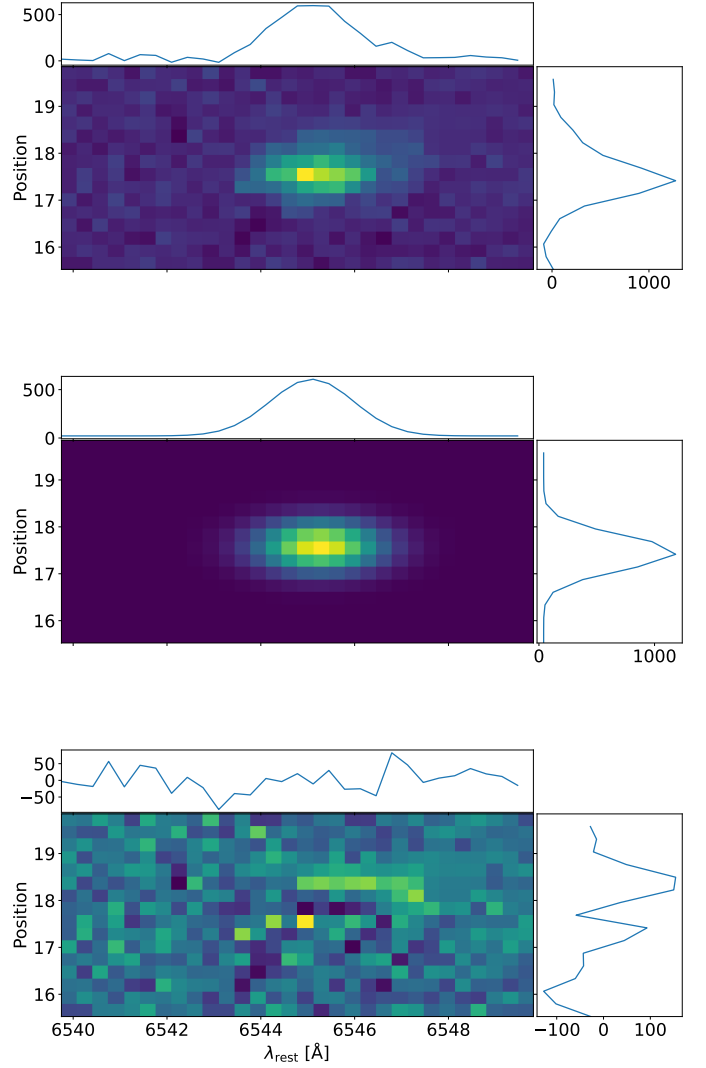


Figure 4. 2D medium resolution LRIS spectrum of the host galaxy of FRB 121102. Wavelength has been converted to the rest frame using the previously reported redshift of $z = 0.19273$ (Tendulkar et al. 2017). Top to bottom panels are the observed 2D spectrum, the 2D fitting model and the residual (data–model), respectively. On the top and right of each panel are plots of the data collapsed along the wavelength axis and position axis, respectively.

We then determine the width of the instrumental broadening effects by collapsing the 2D spectrum into 1D and fitting each of the three isolated sky lines in the field with a 1D Gaussian function plus an offset. The instrumental spectral broadening width is given by the weighted mean of the three sky lines' $1-\sigma$ widths ($0.638725 \pm 0.000039 \text{ \AA}$). The natural broadening width of the $H\alpha$ line is known to be 0.46 m\AA (e.g. Rybicki & Lightman 1979). The $1-\sigma$ width of the line is

$0.6265 \pm 0.0021 \text{ \AA}$ after quadratically removing the instrumental and natural broadening effects.

The rest frame line width of a Maxwellian velocity distribution (i.e. Gaussian along the line-of-sight) is given by (Rybicki & Lightman 1979):

$$\frac{\Delta\nu}{\nu_0} = \frac{1}{c} \left(\sigma_v^2 + \frac{2kT}{m_H} + v_{\text{turb}}^2 \right)^{1/2} \quad (1)$$

Here, $\Delta\nu$ Hz is the rest-frame line width (1σ) in frequency and $\nu_0 = 4.57 \times 10^{14}$ Hz is the frequency of the H α emission in vacuum. σ_v is the velocity dispersion due to gravity, $\sqrt{2kT/m_H} \approx 12.8$ km/s is the most probable thermal velocity assuming a gas temperature of 10^4 K (e.g. Draine 2011). v_{turb} , the turbulent velocity, is weakly constrained to be $\lesssim 10^3$ km/s as inferred from the scattering measurements of FRB 121102 (Table 2 of Simard & Ravi 2021). We ignored its contribution and find an upper limit of $\sigma_v \lesssim 30$ km s $^{-1}$.

Assuming that the FRB 121102 host galaxy has a central BH, we estimate its mass using the empirical M- σ relation reported in recent literature. The BH mass is $7.8_{-5.2}^{+8.2} \times 10^4 M_\odot$ using the relation derived from a sample of 88 AGN covering a stellar velocity dispersion σ_* of 30 – 268 km s $^{-1}$ (Greene & Ho 2006, error bars calculated from the intrinsic scatter found in the relation). A consistent BH mass of $8.8_{-5.8}^{+16.2} \times 10^4 M_\odot$ is found using the relation based on 93 low-mass active galaxies (Xiao et al. 2011, σ_* from 31 to 138 km/s). Other reports show similar results, though an extrapolation of the M- σ relation is required as the sampled objects cover higher σ_* : the mass is $4.2_{-2.7}^{+7.5} \times 10^4 M_\odot$ (error bars from the intrinsic scatter in the relation) based on a sample of 49 BH mass dynamical measurements in spiral galaxies, S0 galaxies and elliptical bulges ($\sigma = 67$ –385 km s $^{-1}$; Gültekin et al. 2009), and $\sim 10^4 M_\odot$ from 72 similar objects ($\sigma = 75$ – 347 km s $^{-1}$; Ferrarese & Ford 2005; McConnell & Ma 2013). Finally, we note that the measured velocity dispersion is lower than any of those measured from a sample of 35 tidal disruption events host galaxies ($\sigma > 43$ km/s) reported by Wevers et al. 2019, 2017. This suggests that the BH mass in the FRB 121102 host is lower than the BH masses of the tidal disruption event galaxy sample.

We consider two potential errors in our BH mass estimation. First, the H α velocity dispersion measurement may not be suitable for the dynamical analysis. The BH mass is usually estimated from the stellar velocity dispersion measured from multiple absorption lines from an optical or IR spectrum. In our observation, these stellar absorption line widths were unavailable due to the limited SNR. Instead, we infer the velocity dispersion from the line width of a single compact H α emission region

(radius $< 0''.24$ at 1σ , Kokubo et al. 2017) that is offset from the stellar continuum centroid of the galaxy by $0''.29 \pm 0''.05$ (Tendulkar et al. 2017). The H α line width reveals the dynamics of the partially ionized warm star forming gas formed in discrete clouds. If the gas pervades in the galaxy, it is expected to have larger velocity dispersion than the stars due to turbulent motions and provide an upper limit to the BH mass. However, the H α region is isolated to one part of the host and may not represent the global gas dynamics in the host. This could lead to systematic errors as reported in the dynamical analyses of galaxies with irregular gas and dust distributions (Ho et al. 2002).

However, the dynamical mass implied by the H α velocity dispersion is comparable to the stellar mass of the FRB 121102 host galaxy inferred using the optical/IR spectral energy distribution. We assume that the system is virialized for an order-of-magnitude estimation. In an ellipsoid, the kinetic energy is dominated by random motions. The virial theorem gives a total stellar mass of $M_* \sim \sigma_v^2 R_{\text{eff}}/G \sim 10^8 M_\odot$, adopting a half-light-radius of $R_{\text{eff}} = 0.68$ kpc (Bassa et al. 2017). In a pure rotational disk (e.g. disk of a spiral galaxy), a comparable value is expected. The inferred mass is consistent with the stellar mass reported by Bassa et al. (2017) from a spectral energy distribution fit ($(1.3 \pm 0.4) \times 10^8 M_\odot$). This suggests that the velocity dispersion may be useful for the dynamical BH mass estimation. We also note that QRS121102 is spatially associated with the H α emission region.

Second, the M- σ relations could be less reliable at our velocity dispersion for two reasons. (1) Most reports derive the empirical M- σ relation based on a sample of more massive galaxies with larger stellar velocity dispersions. It is unclear how well the relation extends to lower velocity dispersions. (2) Even in the few reports that cover velocity dispersions down to 30 km/s, the M- σ relation is still less reliable due to the larger uncertainty in the empirical mass-luminosity (M-L) relation at the lower end. To derive the M- σ relation, the dynamical mass of the BHs were estimated using the virial relation, where the virial radius is either measured directly from reverberation mapping (e.g. Peterson 1993) or indirectly from the empirical M-L relation that was derived from the reverberation mapped AGN. At the low-mass end, few AGN have been reverberation mapped, so an extrapolation of the M-L relation has to be made in the BH mass estimations, introducing extra uncertainty to the resulting M- σ relation. The M- σ relation might be flatter at the lower-mass end based on a few intermediate mass BHs in the sample (e.g. Greene & Ho 2006),

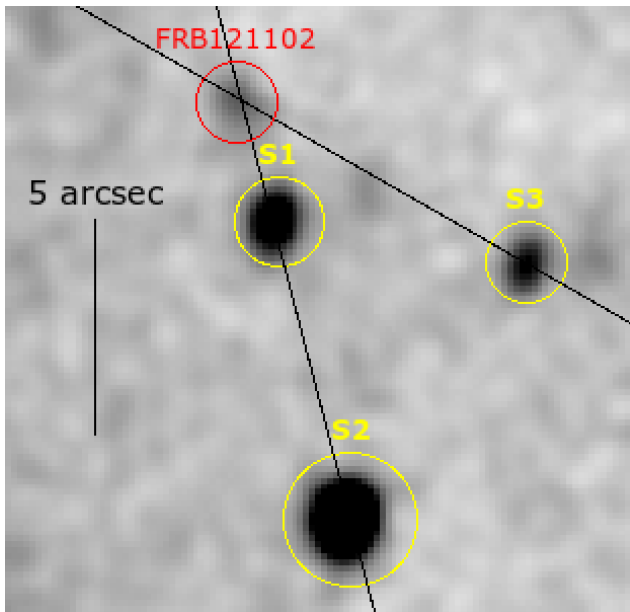


Figure 5. Locations of the host, the slits and the sources in the low resolution Keck/LRIS observation. The slit orientations are shown as black lines. Spectra were extracted for each of sources S1, S2, and S3, together with the FRB 121102 host. The background image is an LRIS *R*-band exposure, as presented in Tendulkar et al. (2017)

although the flattening is inconclusive without reverberation mapping results of the lower-mass BHs.

We validate our BH mass estimation result by comparing to the empirical BH-galaxy mass correlation. Reines & Volonteri (2015) measure the correlation between galaxy stellar mass and BH mass based on a sample of 341 AGN host galaxies, including a sub-sample of dwarf galaxies (Reines et al. 2013). They find that $\log(M_{\text{BH}}/M_{\odot}) = 7.45 + 1.05 \log(M_{*}/10^{11}M_{\odot})$, with a scatter of 0.55 dex. A stellar mass of $10^8 M_{\odot}$ gives an AGN BH mass of $10^{4\sim 5} M_{\odot}$ (1σ uncertainty assuming log-normal mass distribution), consistent with our BH mass estimation.

3.3. Keck/LRIS Low Resolution Spectral Analysis

Data were obtained with two longslit orientations (shown in Fig. 5). The LRIS data were bias subtracted, flattened, cosmic-ray removed, skyline subtracted and flux calibrated using the LPipe (Perley 2019). The LPipe wavelength calibration failed on the red side, since the arc lamps spectrum missed too many of the expected reference lines. We calibrated the wavelength manually by fitting the sky spectra to six isolated, bright skylines. We then selected all nearby sources for which reliable spectra could be extracted—two sources near the host on slit 1 (S1, S2) and one on slit 2 (S3) (Fig. 5).

In this section, we evaluate whether or not the host and its nearby sources belong to the same galaxy group. The redshift of each spectrum was estimated as follows. The procedures were also tested on several SDSS spectra and yield results within 1% of the known redshift values.

1. Remove strong sky line features and data near the boundaries of the wavelength coverage.
2. Interpolate and smooth the spectrum using a 1D Gaussian kernel ($\sigma = 3 \text{ \AA}$) to reduce random high-frequency noise. The kernel width was chosen such that it is narrower than the spectral line width at 8000 \AA ($1\sigma \sim 5 \text{ \AA}$) for a typical galactic velocity dispersion of $\sim 200 \text{ km/s}$ (e.g. Honma et al. 2012). Somewhat different kernel width choices (1 \AA , 3 \AA , 5 \AA) do not change the redshift results significantly.
3. Fit for the continuum and subtract from the spectrum. The fit was done using the *Astropy* package *specutils*, which removes spikes using a median filter and fits the spike-removed spectrum with a list of models using the Levenberg-Marquardt algorithm.
4. Extract a 60-\AA -long segment of spectrum centered at each typical galaxy absorption (or emission) line and stack them. We considered the following absorption lines as they are near the visible wavelength at a redshift of ~ 0 to 1: the Balmer series, Ca K&H (3934.777, 3969.588), the G-band (4305.61), Mg (5176.7), Na (5895.6), and Ca[II] (8500.36, 8544.44, 8664.52). We ignored emission lines since none of our sources show significant emission features. The segment width of 60 \AA was chosen such that it were able to include at last the $\pm 5\sigma$ region of a spectral line broadened by a typical galactic vlocity dispersion of 200 km/s (e.g. Honma et al. 2012), but not too wide to contain multiple lines.
5. Compare the amplitude of the stacked segment at a grid of trial redshift values. In this work, the best estimation occurs at the deepest valley since we only considered absorption lines.

For S1, we find $z \approx 0.5796$ and inspect absorptive features at the wavelengths of the Ca H&K, Mg, H γ and possibly the G-band. For S2, we find $z \approx 0.4471$ and see absorptive features at the wavelengths of the Ca K, the G-band, Na, and potentially H α . For S3, a few weak lines (the Ca H, Mg and Na) indicate that this source might be close to S2 in redshift, but we were unable to reach a conclusion due to the low SNR. We find no

significant spectral feature at the expected wavelengths assuming that S3 were at the host redshift. None of the three sources is likely to be at the same redshift as the host of FRB 121102.

4. DISCUSSION

4.1. Does QRS121102 scintillate?

4.1.1. Scattering theory predictions

Compact sources scintillate as their wavefronts propagate through an inhomogeneous ionized medium. Within the medium, fluctuations in the electron density lead to variations of the refractive index, which change the phase of the wavefront. The fluctuations can be described by the phase structure function defined as the phase difference of two points separated by a distance x :

$$D_\varphi(x) = \langle [\varphi(x+x_0) - \varphi(x)] \rangle_{x_0} \propto x^\alpha. \quad (2)$$

Here, α is 5/3 for Kolmogorov turbulence (Armstrong et al. 1995). We adopt a Kolmogorov turbulence assumption in our calculations thereafter. When there are relative motions between the source, the medium and the observer, the fluctuations cause temporal variations in the observed flux density.

For extragalactic sources, scattering is dominated by the Milky Way ISM, which can often be approximated as a thin scattering screen at a distance D from the observer (e.g., Romani et al. 1986). One characteristic property of the screen is the Fresnel scale (e.g. Narayan 1992),

$$r_F = \sqrt{\frac{\lambda D}{2\pi}}, \quad (3)$$

which is the transverse length at which the phase of a wavefront with wavelength λ changes by one radian due to the geometric path length difference, assuming that $D \gg \lambda$. The corresponding angular radius of the first Fresnel zone is given by

$$\theta_F = \sqrt{\frac{c}{2\pi\nu D}}. \quad (4)$$

Here, c is the speed of light and ν is the wave frequency. Another feature of the scattering screen is r_0 , the transverse scale at which the phase changes by one radian due to the ISM free electron inhomogeneities. Based on the relation of these two scales, scattering is divided into the weak regime ($r_0 \gg r_F$) and the strong regime ($r_0 \ll r_F$). The transitional frequency, ν_0 , is defined as the frequency at which $r_0 \sim r_F$ for an extragalactic source. We estimate that $\nu_0 = 38$ GHz along the line of sight of FRB121102 ($l \approx 175^\circ$, $b \approx -0.2^\circ$) using the NE2001 electron density model (Cordes & Lazio 2002, 2003). Our observations were taken at frequencies (12

to 26 GHz) below ν_0 , so they all belong to the strong scattering regime.

In the strong scattering regime, there are two main types of scintillation behaviors: refractive and diffractive. We summarize the predicted scintillation behaviors below based on Romani et al. (1986) and Walker (1998).

Diffractive scintillation is produced by interference effects between light rays passing through small-scale ($\ll r_F$) ISM inhomogeneities. The variations are fast ($t_d \sim 2(\nu/\nu_0)^{6/5} \sim 5$ hours at $\nu = 18$ GHz) and narrow-band ($\Delta\nu \approx \nu(\nu/\nu_0)^{17/5} \approx 1$ GHz at $\nu = 18$ GHz).

In contrast, refractive scintillation is caused by large-scale ($\gg r_F$) ISM inhomogeneities. The observed flux density variability is slow and broad-band. For Kolmogorov turbulence, the angular radius of the apparent scattering disc at frequency ν is

$$\theta_r = \theta_{F0} \left(\frac{\nu_0}{\nu} \right)^{11/5}. \quad (5)$$

Here, θ_{F0} is the angular size of the first Fresnel zone at the transitional frequency ν_0 . The observed flux density of a compact source smaller than θ_r varies on a refractive time-scale (in hours) of

$$t_r \sim 2 \left(\frac{\nu_0}{\nu} \right)^{11/5}, \quad (6)$$

assuming a typical relative transverse velocity of 50 km/s (Rickett et al. 1995). In this work, modulation index is defined as the weighted root-mean-square (rms) fractional variation:

$$m_p = \frac{1}{\langle f \rangle} \sqrt{\frac{\sum_i w_i (f_i - \langle f \rangle)^2}{\sum_i w_i}}. \quad (7)$$

Here, f_i is the flux density of the i -th epoch, $w_i = 1/\sigma_{f_i}^2$ is the weight calculated from the measurement uncertainty σ_{f_i} , and $\langle f \rangle$ is the weighted mean flux density. The modulation index of a source smaller than θ_r is given by

$$m_p = \left(\frac{\nu}{\nu_0} \right)^{17/30}. \quad (8)$$

When the point source approximation fails ($\theta_s > \theta_r$, where θ_s is the source angular radius), the modulation index reduces as $m = m_p(\theta_r/\theta_s)^{7/6}$ and the variability timescale increases as $t = t_r(\theta_s/\theta_r)$.

Table 4 lists the predicted θ_r , m_p and t_r using the central frequency of each band, and assuming a point source. We do not predict the substantially larger effects of diffractive scintillation because, as will be seen below, we observe significantly less modulation than expected

Table 4. Predicted Galactic Refractive Scintillation Properties of QRS121102 Assuming a Point Source and Kolmogorov Turbulence

Band (ν_c)	m_p	t_r	θ_r ^a
		(Hour)	(μ as)
K (22 GHz)	73%	~ 7	4
U (15 GHz)	59%	~ 16	10

^a Assuming a nominal distance between the scattering screen and the observer to be 1 kpc.

due to refractive scintillation alone. We calculate θ_r (eqn. 4, 5) using a distance D ranging from 100 pc to 10 kpc (Fig. 6), and list the θ_r corresponding to a nominal distance of 1 kpc (\sim galactic scale height) in Table 4. For scattering media dominated by a steeper fluctuation spectrum, the expected values of m_p , t_r and θ_r would be greater (Armstrong et al. 1995).

4.1.2. Comparison between the flux density measurements and predictions

In the following analyses, we analyze two types of flux density measurements in each band—

- The normalized flux density measurements of QRS121102 (“ $f3$ ” in Table 5).
- The flux density measurements of QRS121102 divided by those of J0518+3306 and then normalized (“ $f3/f2$ ” in Table 5). The scaling is justified for two reasons. (1) The phase calibrators J0518+3306 (and J0518+3306) are not expected to scintillate, since the constraints on their angular radii and the observed flux densities would require a brightness temperature exceeding the inverse Compton catastrophe threshold $\gtrsim 10^{12}$ K (and $\gtrsim 10^{13}$ K)—assuming a scattering screen at 1 kpc. (2) The variations are unlikely to be intrinsic due to the strong correlations and the short variation timescale, as explained in Section 3.1.

We calculate the modulation indices of the above four sets of flux density measurements (Table 5, column 3) and find each of them more than 5σ lower than the predictions (error bar calculated from the statistical errors in the flux density measurements), though our observation spacings are longer than the predicted refractive time scale (Table 4). To conclude the comparison, we perform χ^2 tests for two hypotheses —

1. The flux density is constant.
2. The flux density measurements are drawn from a Gaussian distribution whose modulation is equal to the scattering theory prediction (Table 4, Section 4.1.1). A Gaussian distribution is used here to provide a conservative test, though galactic scattering has been observed to modulate intensity with one-side exponential functions (e.g. Cordes 2002).

We test the first hypothesis by fitting our measurements in each band with their weighted average and calculate the χ^2 :

$$\chi^2 = \sum_i \frac{(f_i - \langle f \rangle_w)^2}{\sigma_{f_i}^2}. \quad (9)$$

Here, $\langle f \rangle_w$, f_i and σ_{f_i} are the weighted average flux density, the i -th epoch flux density and its measurement error, respectively. For example, in the K-band, the best-fit result of $f3/f2$ has a χ^2_{\min} of 5.8 and a degree of freedom (dof) of 2, yielding a one-side P-value of 5.6% for obtaining a χ^2_{\min} that is greater or equals to our observation if the flux density were constant. Other results are listed in Table 5. In both bands, the constant flux density hypothesis is questionable using the $f3/f2$ light curve, and is rejected to a level of at least 10^{-3} using the $f3$ light curve.

We test the second hypothesis by simulating 10^5 light curves for both bands, each with the same number of measurements and the same fractional uncertainties as our observations. For each light curve, the flux densities are drawn from the absolute values of a Gaussian distribution centered at unity and with a standard deviation of $m_p \sqrt{n/(n-1)}$, where m_p is the expected modulation index and n is the number of measurements. We calculate the χ^2_ν for each light curve and compare the smoothed distribution with our observations in each band. For example, using $f3/f2$ in the Ku-band, $\sim 3\%$ of the simulated light curves have χ^2_ν values lower than or equals to our observation (2.9), questioning the second hypothesis. In both bands, the scintillation-variability-hypothesis is doubtful using the $f3/f2$ data.

4.1.3. Implications

We have found it questionable that our observation is consistent with refractive scintillation predictions for a point-like source. We will discuss the implications of the absence of refractive scintillation modulation in our observations.

First, scintillation variations would be smeared out if the angular size of the source is greater than that of the

Table 5. VLA Flux Density Modulation Indices Results and Statistical Tests

Data (band)	m'_p (Observed)	χ^2_{\min} (dof)	Constant $P(\geq \chi^2_{\min}; \nu)$	Refractive Scintillation $P(\leq \chi^2_{\nu}; m_p)$
$f3/f2^a$ (K)	$(19.3 \pm 7.1)\%$	5.8 (2)	5.6%	$\sim 9\%$
$f3/f2$ (U)	$(13.3 \pm 4.8)\%$	10.9 (3)	1.2%	$\sim 3\%$
$f3^b$ (K)	$(30.2 \pm 5.8)\%$	13.9 (2)	10^{-3}	$\sim 20\%$
$f3$ (U)	$(26.1 \pm 4.4)\%$	48.5 (3)	10^{-10}	$\sim 23\%$

^aThe flux density measurements of QRS121102 divided by those of J0518+3306 and then normalized to an average of unity.

^bThe normalized flux density measurements of QRS121102.

Table 6. Implications of the lack of refractive scintillation.

Observation	$\langle f_\nu \rangle^a$ (μJy)	Radio Luminosity ^b (erg s^{-1})	Radius ^c (cm)	T_b^c (k)
VLA K-band (22 GHz)	61.3 ± 5.0	1.5×10^{39}	$\gtrsim 10^{17}$	$\lesssim 5 \times 10^8$
VLA Ku-band (15 GHz)	89.4 ± 3.4	1.5×10^{39}	$\gtrsim 4 \times 10^{16}$	$\lesssim 2 \times 10^9$

^aWeighted Average Flux Density

^bIsotropic Luminosity $L \approx \nu_c \langle f_\nu \rangle 4\pi D_L^2$, where ν_c is the band central frequency.

^cAssuming a nominal distance of 1 kpc between the scattering screen and the observer.

scattering disc. The lack of modulation implies a lower limit to the physical size of the source in each band (Fig. 6). Here, the scattering disc angular size lower limit is calculated assuming a range of distances from 100 pc to 10 kpc between the scattering screen and the observer. The physical size limit of the source is obtained using the angular size limit and the host redshift ($z = 0.19273$). In the Ku-band, the scattering disc radius is $10 \mu\text{as}$ (Table 4) assuming a scattering screen distance of 1 kpc (\sim galactic scale height), corresponding to a physical radius of $R \gtrsim 10^{17}$ cm (0.03 pc) at the host redshift. This together with the VLBI resolution at 5 GHz limit the emission radius to be between $\sim 10^{17}$ cm and $\sim 10^{18}$ cm. Alternatively, a rough estimation on the source radius could be made using the measured modulation index. When the angular radius of the source is larger than that of the refractive scattering disc, the variability would reduce and the source radius is given by $\theta_s \approx \theta_r (m_p/m'_p)^{6/7}$, where m_p is the expected scintillation modulation index, m'_p is the observed modulation index and θ_r is the refractive scintillation disc angular radius. This gives a source radius of $14 \mu\text{as}$ (1.4×10^{17} cm) in the K-band and $36 \mu\text{as}$ (3.7×10^{17} cm) in the Ku-band

(using the host redshift and assuming a scattering screen at 1 kpc), within the above constraints of $10^{17\sim 18}$ cm.

In addition, the constraint on source size rules out the scenario that the flux density modulation is intrinsic. The flux density varies significantly within a week in the Ku-band (e.g. epochs 3, 4, 5). If the modulations were intrinsic, the source radius would be $R \lesssim (1/2) \cdot (7 \text{ days}) \cdot c \sim 10^{14}$ cm, three orders of magnitude below the scintillation size limit. The source would also have scintillated more if the fast variations were intrinsic.

Moreover, the brightness temperature of the source can be constrained by its size limit and flux density measurement. Brightness temperature provides clues on the radio emission process. For example, a brightness temperature above 10^5 K may rule out star-forming galaxies (e.g., Condon 1992), and a brightness temperature above 10^{12} K requires coherent processes or relativistic boosting (e.g., Rybicki & Lightman 1979). The brightness temperature is given by:

$$T_b \lesssim \frac{fc^2}{2\pi\theta_{r,15\text{GHz}}^2 k_b \nu^2}. \quad (10)$$

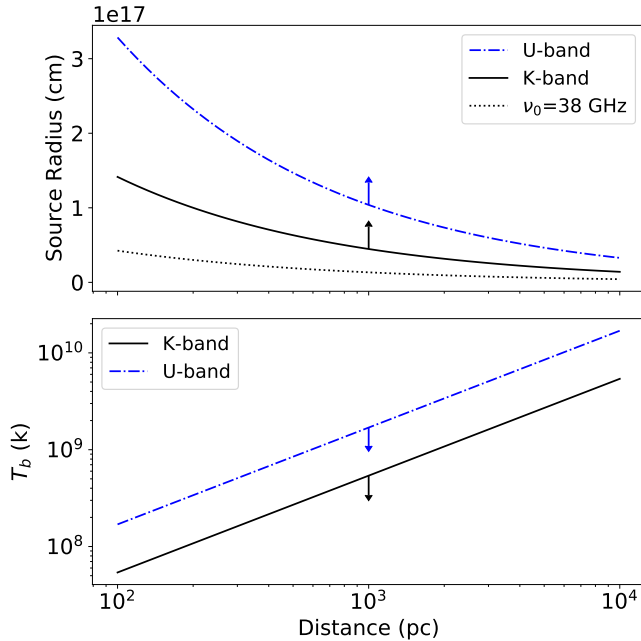


Figure 6. Implication from the lack of refractive scintillation modulation assuming a range of distances between the scattering screen and the observer. Upper panel: source radius lower limits in the Ku-band (dashed blue line) and the K-band (solid black line), as well as the size of the scattering disc at the transitional frequency ν_0 . Lower panel: brightness temperature upper limits using the emission region size lower limit inferred from the Ku-band ($\theta_r \gtrsim 10 \mu\text{as}$) and the weighted average flux densities measured in the Ku-band (dashed blue line) and the K-band (solid black line).

Here, $\theta_{r,15\text{GHz}}$ is the radius lower limit implied by the lack of scintillation modulation in the Ku-band, and ν is the frequency at which the flux density f is measured. Assuming a scattering screen distance of 1 kpc (Table 6), we find $T_b \lesssim 5 \times 10^8 K$ using our average flux density measured in the K-band ($\nu_c = 22 \text{ GHz}$, $\langle f_\nu \rangle \approx 61.3 \pm 5.0 \mu\text{Jy}$, weighted by the statistical errors in the flux density measurements) and $T_b \lesssim 2 \times 10^9 K$ using the weighted average flux density measured in the Ku-band ($\nu_c = 15 \text{ GHz}$, $\langle f_\nu \rangle \approx 61.3 \pm 5.0 \mu\text{Jy}$). A more complete result assuming a range of scattering screen distances is shown in Fig. 6.

4.2. Optical

4.2.1. Implications of Constraint on Potential supermassive BH Mass

We have estimated the mass of the potential supermassive BH to be $10^{4\sim 5} M_\odot$ using the velocity dispersion measured from the $\text{H}\alpha$ emission line width (section 3.2). We will test the AGN hypothesis by comparing its

mass, radio luminosity and X-ray luminosity with the AGN population.

The radio luminosity of QRS121102 is several orders of magnitude higher than expected given $M_{BH} \approx 10^{4\sim 5} M_\odot$, based on results from a large sample of AGN with higher BH masses (Lacy et al. 2001). However, it may not be rare in a sample of bright radio emissions detected in dwarf galaxies at intermediate redshifts (Mezcua et al. 2019), and is only slightly brighter than those detected in some nearby dwarf galaxies (Reines et al. 2020). For the general AGN population, the BH mass (M_{BH}), radio luminosity ($L_{5\text{GHz}}$), and the ratio of bolometric luminosity to the Eddington limit (L/L_{Edd}) has been reported to be correlated. For example, Lacy et al. (2001) measure a relation based on a sample of 60 AGN with BH masses of $10^{6.5\sim 10} M_\odot$: $\log_{10}(L_{5\text{GHz}}) = 1.9 \log_{10}(M_{BH}/M_\odot) + x \log_{10}(L/L_{Edd}) + 7.9$ (with a scatter of 1.1 dex), where $L_{5\text{GHz}}$ is in a unit of $\text{W Hz}^{-1} \text{sr}^{-1}$, $x \approx 1$ for a typical (L/L_{Edd}) of 0.1 and $x \approx 0.3$ for a low (L/L_{Edd}) of 10^{-5} . The specific radio luminosity of QRS121102 is $L_{5\text{GHz}} \approx 10^{21.2} \text{ W Hz}^{-1} \text{sr}^{-1}$, as calculated using the host redshift and the flux density of $\approx 200 \mu\text{Jy}$ at 3GHz and 6 GHz (Chatterjee et al. 2017). This is three orders of magnitude greater than calculated from the relation (scatter included) even if $L/L_{Edd} = 100\%$ and $M_{BH} = 10^5 M_\odot$. However, we note that the relation reported in Lacy et al. (2001) is derived from a sample of more massive BHs ($10^{6.5\sim 10} M_\odot$).

It is intriguing that the radio luminosity of QRS121102 is consistent with a sample of bright radio emissions detected in dwarf galaxies at intermediate redshifts (Mezcua et al. 2019). The specific radio luminosity of QRS121102 at 3 GHz is $L_{3\text{GHz}} \sim 2.3 \times 10^{22} \text{ W Hz}^{-1}$, as calculated using the host redshift and the flux density at 3 GHz ($206 \pm 17 \mu\text{Jy}$; Chatterjee et al. 2017). This lies within the broad luminosity range ($L_{3\text{GHz}} \approx 10^{21.5\sim 24.2} \text{ W Hz}^{-1}$) observed in a sample of 35 dwarf galaxies ($10^7 < M_* < 10^{9.5}$) at intermediate redshifts (0.13 to 3.4) hosting compact radio sources from the VLA-COSMOS 3 GHz Large Project catalog (Mezcua et al. 2019). These sources are suspected to be AGN mainly because they are significantly more luminous ($\geq 2\sigma$) than expected from star formation processes. In particular, a few objects in their sample show similar radio luminosities, host stellar masses, BH mass estimations and redshifts with QRS121102, although the constraints on their X-ray luminosities are weaker (Table 1, 2 of Mezcua et al. 2019). Similarly, the specific luminosity at 10 GHz ($\sim 1.9 \times 10^{22} \text{ W Hz}^{-1}$) is only slightly above the observed range ($10^{18.5\sim 22} \text{ W Hz}^{-1}$) from 13 nearby ($z < 0.055$) dwarf galaxies hosting bright radio sources that are too bright to be star formation processes or su-

pernova remnants (Reines et al. 2020). We suggest that the nature of several of these radio sources, including QRS121102, remains uncertain (e.g., Law et al. 2021).²

In addition, we estimate the minimum average radio luminosity of QRS121102 during its past life span and find it uncomfortably high given constraints on the X-ray luminosity. We assume possible source radii of 10^{17} cm (lower limit from this work) and 10^{18} cm (upper limit from the previous VLBI observation; Marcote et al. 2017) and calculate the minimum energy (equipartition energy) based on section 2.3 of Vedantham & Ravi 2019. Assuming a power-law electron energy distribution of index -1.5 (to enable direct comparison with Vedantham & Ravi 2019 and to account for the flat spectrum), the minimum total energies required to power a synchrotron source with the observed radio luminosity at these two size limits are $E_q \approx 10^{48.9}$ ergs ($B_{\text{eq}} \approx 27$ mG) and $\approx 10^{50.2}$ ergs ($B_{\text{eq}} \approx 190$ mG), respectively (e.g. Chapter 5 of Condon & Ransom 2016). Adopting a conservative expansion speed of $\sim 0.01c$ (Vedantham & Ravi 2019), the average radio luminosity during its past lifespan would be 2×10^{40} erg s⁻¹ (5×10^{40} erg s⁻¹), about 0.2% (0.5%) of the Eddington limit for a $10^5 M_\odot$ BH. This is uncomfortably high, accounting for typical amounts ($\sim 10\%$) of energy deposited into relativistic electrons, given the upper limit on X-ray emission of 4% of the Eddington limit for a $10^5 M_\odot$ BH (Chatterjee et al. 2017).

The radio and X-ray observations of QRS121102 can also be compared with the radio / X-ray luminosity correlation in accreting BH systems (e.g. Hannikainen et al. 1998). In particular, the AGN BH mass has been found to be correlated with its radio and X-ray luminosity (e.g. Falcke et al. 2004; Merloni et al. 2003). A recent report based on a sample of 30 AGN with independent dynamical mass measurements shows that $\log(M/10^8 M_\odot) = 0.55 + 1.09 \log(L_R/10^{38} \text{erg s}^{-1}) - 0.59 \log(L_X/10^{40} \text{erg s}^{-1})$ (Gültekin et al. 2019), with a 1σ scatter of 1 dex assuming a log-normal mass distribution. Here, L_R and L_x are the luminosity at 5 GHz and 2 to 10 keV, respectively, observed within close epochs ($\Delta t \lesssim 2 + M/10^6 M_\odot$ days). We adopt a 5 GHz flux density of $f_R \approx 5 \text{ GHz} \cdot 200 \mu\text{Jy} \sim 10^{-17} \text{erg s}^{-1} \text{cm}^{-2}$ measured by VLA and an X-ray flux upper limit of $f_x \lesssim 5 \times 10^{-15} \text{erg s}^{-1} \text{cm}^{-2}$ inferred from the non-detection in the XMM-Newton and Chandra images (Chatterjee et al. 2017). We convert the flux density to isotropic luminosity using the host redshift and have

$L_R \approx 10^{39} \text{erg s}^{-1}$ and $L_x \lesssim 5 \times 10^{37} \text{erg s}^{-1}$, giving a BH mass of $\sim 10^{11} M_\odot$, 6 ~ 7 orders of magnitude greater than our measurement. Therefore the persistent radio source does not follow the AGN BH mass-luminosity relation measured in Gültekin et al. (2019).

4.2.2. AGN in an Isolated Dwarf Galaxy

A fraction (8% to 32%) of supermassive BH have been estimated to reside within high mass ultra-compact dwarf galaxies, suggesting that some of those galaxies could be the stripped cores of larger galaxies through tidal interactions with their companions (Voggel et al. 2019). We find that this scenario is not supported for QRS121102 for two reasons. First, the low BH mass estimated from the gas velocity dispersion is consistent with a typical dwarf galaxy instead of a more massive galaxy (section 3.2). Second, member(s) from the same galaxy group are expected to be associated with QRS121102 if the host had been dynamically stripped by nearby companions. From the low resolution LRIS spectra, we found that the three nearby bright sources are likely to have different redshift values from the host (section 3.3).

We extend this argument by searching the PanSTARRS catalog for potential companions that are likely to belong to the same galaxy group. We search the PanSTARRS catalog for sources within 5 arcmin (~ 1 Mpc, the virial radius of a galaxy group with a typical mass of $\sim 10^{13} M_\odot$ and velocity of 200 km/s) and have consistent photometric redshift measurements with the host. One object (PSO J082.9850+33.0967) was found at 3' from QRS121102 but only detected in a stacked image and have no valid magnitude measurement available in the catalog. Another object (PSO J082.9961+33.0895) was ignored due to the large uncertainty in its photometric redshift (0.20 ± 0.18). We find no promising group member candidate from the PanSTARRS catalog. Moreover, we compare the PanSTARRS galaxy number density within this area with the galaxy number density calculated from the deep VRI images in the R-band produced by the Keck Telescope (Smail et al. 1995). In that work, they estimate a galaxy number density of $\approx 7 \times 10^5 \text{deg}^{-2}$ with a magnitude range of $20.5 \lesssim m_R \lesssim 27.2$. In the PanSTARRS DS1 catalog, 2705 objects are found within a radius of 5 arcmin around FRB121102, and 30 of them are classified as galaxies above a confidence level of 90% (Tachibana & Miller 2018). The limiting magnitude of PanSTARRS is $m_r \approx 23.2$, six times shallower than that of the deep VRI images, predicting ≈ 60 galaxies within the searched area at a limiting magnitude of 23.2. The galaxy number density near QRS121102 is not overdense compare to an average sky

² Although see Molina et al. 2021 for an example of an unambiguous AGN in a dwarf galaxy.

region. We find no evidence that the host belongs to a galaxy group.

4.3. What Else Could the Source Be

We have found that QRS121102 is unlikely to be an AGN based on the low inferred BH mass ($\lesssim 10^{4\sim 5} M_\odot$), high radio-to-X-ray luminosity ratio and the absence of companions from the same galaxy group. In this section, we discuss other possible sources for the compact persistent radio emission.

The size of the persistent radio emission could be explained by an isolated young neutron star with luminous synchrotron emission produced in a pulsar wind nebula (PWN), or plerion. The pulsar wind forms a terminal shock at a radius where the wind momentum flux and the confining pressure reach a balance, and forms a PWN further out. The shock radius is given by: $r_w = \sqrt{\dot{E}/(4\pi\eta cp)}$ (Slane 2005), where \dot{E} is the pulsar energy injection rate into the wind, η is the fraction of area covered by the wind, c is the speed of light, p is the confining pressure outside the shock and is proportional to the electron number density n_e for medium with the same components. The relation gives a radius of ~ 0.1 pc for a canonical isolated radio pulsar, and is confirmed to be $\approx 3 \times 10^{17}$ cm from the X-ray images of the Crab nebula (Weisskopf et al. 2000). For the Crab pulsar, the spin down energy rate is $\dot{E} \sim 4.5 \times 10^{38}$ ergs s^{-1} (Staelin & Reifenstein 1968), and the confining pressure outside the shock is proportional to the density of the medium, which can be approximated as a typical ISM ($n_e \sim 10^{-1}$ to 10^{-2} cm^{-3} ; e.g. Draine 2011). In comparison, the energy ejection rate of FRB 121102 by the flares and the wind into the surrounding medium is estimated to be $\dot{E} \sim 10^{39}$ to 10^{40} ergs s^{-1} (Fig. 5 of Margalit et al. 2020), and the medium ahead of the termination shock is likely denser than a typical ISM, as indicated from the high RM of FRB 121102 (Michilli et al. 2018).

One example of the PWN emission model that produce the observed radio luminosities and the size of QRS121102 is presented in Margalit & Metzger (2018), where the authors explain the persistent emission using a concordance FRB model. On a large scale ($\sim 10^{15}$ cm, Eqn. 4 of Metzger et al. 2019), the train of ion-electron shells merge into a steady wind and feed into a nebula via a terminal shock, which heats up electrons in the nebula and produces the persistent synchrotron radio source. Based on the lack of self-absorption feature down to 6.0 GHz in the spectrum of the persistent source (Chatterjee et al. 2017), Margalit & Metzger (2018) estimate that the emission region's radius $R \gtrsim 0.46 \times 10^{17}$ cm adopting the observed luminosity

at 6 GHz. Moreover, Resmi et al. (2020) report the lack of self-absorption down to 400 MHz in their GMRT observations. Using their flux density measurement at 400 MHz and the scaling relation $R \propto L_{\nu, \text{obs}}^{4/11} \nu_{\text{obs}}^{-10/11}$ (Eqn. 21 in Margalit & Metzger 2018), we find that $R \gtrsim 5.4 \times 10^{17}$ cm. This emission size is consistent with the constraint implied by the lack of refractive scintillation in the Ku-band.

Among the more unique features of QRS121102 is its unusually flat radio spectrum at GHz frequencies (Chatterjee et al. 2017). As we have noted, several examples of compact radio sources of similar luminosities exist in dwarf galaxies. Indeed, two recent discoveries of *transient* radio sources not associated with BHs also reached similar radio luminosities. The first, FIRST J141918.9+394036, had a peak radio luminosity of 2×10^{29} erg d^{-1} Hz^{-1} at 1.4 GHz, and is hosted by a star-forming dwarf galaxy (Law et al. 2018). FIRST J141918.9+394036 is most likely the afterglow of an off-axis long-duration GRB (Mooley et al. 2021). The second, VT J121001+495647, had a peak radio luminosity of 1.5×10^{29} erg s^{-1} Hz^{-1} at 5 GHz, was associated with a star-forming region, and was ascribed to interaction with a dense circum-stellar medium ejected through binary interaction (Dong et al. 2021). In both cases, however, classical synchrotron spectral shapes were observed together with secular time-evolution, unlike in the case of QRS121102. We urge continued wideband monitoring of QRS121102, together with more detailed evaluation of potential empirical analogs.

Finally, we rule out a few other possible origins of QRS121102 based on our observations. First, the source cannot be a supernova remnant (SNR) due to its high luminosity. We have calculated the specific luminosity of QSR121102 at 3 GHz and 10 GHz as $L_\nu \sim 10^{22}$ W Hz^{-1} . Varenus et al. (2019) and Ulvestad (2009) recently report the radio luminosities (5 GHz and 8.4 GHz) of 102 SNRs in the merging galaxies Arp 220 and Arp 229. The brightest SNR in the sample is $L_\nu < 10^{21}$ W Hz^{-1} , over one order of magnitude lower than that of QSR121102. Moreover, the luminosity is inconsistent with the star formation rate (SFR) of the host galaxy if the source were SNR(s). The brightest SNR and the SFR of a galaxy have been reported to be related (Chomiuk & Wilcots 2009) as: $L_{1.4}^{\text{max}} = 95_{-23}^{+31} \text{SFR}^{0.98 \pm 0.12}$, where $L_{1.4}^{\text{max}}$ is in a unit of 10^{24} erg s^{-1} Hz^{-1} and SFR is in $M_\odot \text{year}^{-1}$. Adopting the SFR upper limit of $0.4 M_\odot \text{year}^{-1}$ based on the host H α emission flux (Tendulkar et al. 2017), the brightest SNR in the host would be $L_{1.4}^{\text{max}} \approx 10^{18.6}$ W Hz^{-1} , over 3 orders of magnitude lower than that of QSR121102. The persistent source is too bright to be an SNR. Second, the source is too

bright for a long-duration GRB (LGRB) radio afterglow. Adopting a typical LGRB peak radio luminosity of $L_{\nu,8.5\text{GHz}} \sim 2 \times 10^{31} \text{ erg}^{-1} \text{ s}^{-1} \text{ Hz}^{-1}$ and a decay rate of $\propto t^{-2}$ from day 10 after the GRB (e.g. Berger et al. 2003), the radio luminosity would have reached the level of QRS121102 ($L_{\nu,10\text{GHz}} \approx 2 \times 10^{29} \text{ erg}^{-1} \text{ s}^{-1} \text{ Hz}^{-1}$) within 3 weeks, while the radio luminosity of QRS121102 have been nearly constant below 10 GHz for years (e.g. Resmi et al. 2020; Tendulkar et al. 2017).

5. CONCLUSION

In this work, we investigated the origin of the persistent radio source, QRS121102, associated with FRB 121102. We present new VLA monitoring data (12 to 26 GHz) and new spectra from Keck/LRIS. The main results are summarized as follows:

1. We constrained the emission radius to be $10^{17\sim 18}$ cm based on the low level of scintillation variability in our VLA observations and the previous VLBI observation. A few compact radio sources (e.g. AGN, PWNs, very young SNRs and GRB afterglows) could fall into these size limits. Most interpretations with the exception of an AGN would have been in tension with a converse finding of significant scintillation in QRS121102.
2. To further investigate the hypothesis that the source is an AGN, we roughly constrained the mass of the potential BH to be $\lesssim 10^{4\sim 5} M_{\odot}$ using the $H\alpha$ velocity dispersion. The radio luminosity ($L_{\nu} \sim 2 \times 10^{22} \text{ W Hz}^{-1}$ from 400 MHz to 10 GHz) is possibly too high at this BH mass compared to the general AGN population, although similarly bright radio emissions have been reported in several dwarf galaxies. The source is also unlikely to

be an AGN because it is too faint in the X-ray for its low BH mass and bright radio emission.

3. A significant fraction of dwarf galaxies hosting supermassive BHs may be the stripped cores of massive galaxies during tidal interactions with their nearby companion(s). From our LRIS spectra and the PanSTARRS catalog, we found no promising companion galaxy near the host to support an environment for a tidal stripping event history.
4. We briefly discussed possible origins other than AGN. QRS121102 is too luminous in the radio band to be an SNR and too old to be a typical GRB afterglow. The isolated young neutron star models for FRBs might be able to account for both the size and the luminosity of the persistent source as synchrotron emission produced in the PWN (e.g. Metzger et al. 2019).

In conclusion, the persistent radio emission associated with FRB 121102 is likely not an AGN, and its nature remains interesting for FRB emission models involving extreme neutron stars.

ACKNOWLEDGMENTS

The authors thank Dr. Casey J. Law for VLA imaging and visualization tips and the catalog querying code *psquery*. We also thank Dr. Casey J. Law and Dr. Liam D. Connor for helpful discussions on PRS and the unknown radio emissions in dwarf galaxies. We thank staff members at the CASA help desk, Dillon Dong and Nitika Yadlapalli for CASA tips. This material is based upon work supported by the National Science Foundation under grant No. AST-1836018.

REFERENCES

- Armstrong, J. W., Rickett, B. J., & Spangler, S. R. 1995, ApJ, 443, 209, doi: [10.1086/175515](https://doi.org/10.1086/175515)
- Baldwin, J. A., Phillips, M. M., & Terlevich, R. 1981, PASP, 93, 5, doi: [10.1086/130766](https://doi.org/10.1086/130766)
- Bassa, C. G., Tendulkar, S. P., Adams, E. A. K., et al. 2017, ApJL, 843, L8, doi: [10.3847/2041-8213/aa7a0c](https://doi.org/10.3847/2041-8213/aa7a0c)
- Berger, E., Kulkarni, S. R., Pooley, G., et al. 2003, Nature, 426, 154, doi: [10.1038/nature01998](https://doi.org/10.1038/nature01998)
- Briggs, D. S. 1995, in American Astronomical Society Meeting Abstracts, Vol. 187, American Astronomical Society Meeting Abstracts, 112.02
- Chatterjee, S., Law, C. J., Wharton, R. S., et al. 2017, Nature, 541, 58, doi: [10.1038/nature20797](https://doi.org/10.1038/nature20797)
- Chomiuk, L., & Wilcots, E. M. 2009, ApJ, 703, 370, doi: [10.1088/0004-637X/703/1/370](https://doi.org/10.1088/0004-637X/703/1/370)
- Condon, J. J. 1992, ARA&A, 30, 575, doi: [10.1146/annurev.aa.30.090192.003043](https://doi.org/10.1146/annurev.aa.30.090192.003043)
- Condon, J. J., & Ransom, S. M. 2016, Essential Radio Astronomy
- Cordes, J. M. 2002, in Astronomical Society of the Pacific Conference Series, Vol. 278, Single-Dish Radio Astronomy: Techniques and Applications, ed. S. Stanimirovic, D. Altschuler, P. Goldsmith, & C. Salter, 227–250
- Cordes, J. M., & Lazio, T. J. W. 2002, arXiv e-prints, astro. <https://arxiv.org/abs/astro-ph/0207156>

- . 2003, arXiv e-prints, astro.
<https://arxiv.org/abs/astro-ph/0301598>
- Cruces, M., Spitler, L. G., Scholz, P., et al. 2021, MNRAS, 500, 448, doi: [10.1093/mnras/staa3223](https://doi.org/10.1093/mnras/staa3223)
- Dong, D. Z., Hallinan, G., Nakar, E., et al. 2021, Science, 373, 1125, doi: [10.1126/science.abg6037](https://doi.org/10.1126/science.abg6037)
- Draine, B. T. 2011, Physics of the Interstellar and Intergalactic Medium
- Falcke, H., Körding, E., & Markoff, S. 2004, A&A, 414, 895, doi: [10.1051/0004-6361:20031683](https://doi.org/10.1051/0004-6361:20031683)
- Ferrarese, L., & Ford, H. 2005, SSRv, 116, 523, doi: [10.1007/s11214-005-3947-6](https://doi.org/10.1007/s11214-005-3947-6)
- Franzen, T. M. O., Davies, M. L., Davies, R. D., et al. 2009, MNRAS, 400, 995, doi: [10.1111/j.1365-2966.2009.15673.x](https://doi.org/10.1111/j.1365-2966.2009.15673.x)
- Greene, J. E., & Ho, L. C. 2006, ApJL, 641, L21, doi: [10.1086/500507](https://doi.org/10.1086/500507)
- Gültekin, K., King, A. L., Cackett, E. M., et al. 2019, ApJ, 871, 80, doi: [10.3847/1538-4357/aaf6b9](https://doi.org/10.3847/1538-4357/aaf6b9)
- Gültekin, K., Richstone, D. O., Gebhardt, K., et al. 2009, ApJ, 698, 198, doi: [10.1088/0004-637X/698/1/198](https://doi.org/10.1088/0004-637X/698/1/198)
- Hannikainen, D. C., Hunstead, R. W., Campbell-Wilson, D., & Sood, R. K. 1998, A&A, 337, 460.
<https://arxiv.org/abs/astro-ph/9805332>
- Ho, L. C., Sarzi, M., Rix, H.-W., et al. 2002, PASP, 114, 137, doi: [10.1086/338546](https://doi.org/10.1086/338546)
- Honma, M., Nagayama, T., Ando, K., et al. 2012, PASJ, 64, 136, doi: [10.1093/pasj/64.6.136](https://doi.org/10.1093/pasj/64.6.136)
- Kokubo, M., Mitsuda, K., Sugai, H., et al. 2017, ApJ, 844, 95, doi: [10.3847/1538-4357/aa7b2d](https://doi.org/10.3847/1538-4357/aa7b2d)
- Lacy, M., Laurent-Muehleisen, S. A., Ridgway, S. E., Becker, R. H., & White, R. L. 2001, ApJL, 551, L17, doi: [10.1086/319836](https://doi.org/10.1086/319836)
- Law, C. J., Connor, L., & Aggarwal, K. 2021, arXiv e-prints, arXiv:2110.15323.
<https://arxiv.org/abs/2110.15323>
- Law, C. J., Gaensler, B. M., Metzger, B. D., Ofek, E. O., & Sironi, L. 2018, ApJL, 866, L22, doi: [10.3847/2041-8213/aae5f3](https://doi.org/10.3847/2041-8213/aae5f3)
- Lorimer, D. R., Bailes, M., McLaughlin, M. A., Narkevic, D. J., & Crawford, F. 2007, Science, 318, 777, doi: [10.1126/science.1147532](https://doi.org/10.1126/science.1147532)
- Marcote, B., Paragi, Z., Hessels, J. W. T., et al. 2017, ApJL, 834, L8, doi: [10.3847/2041-8213/834/2/L8](https://doi.org/10.3847/2041-8213/834/2/L8)
- Margalit, B., & Metzger, B. D. 2018, ApJL, 868, L4, doi: [10.3847/2041-8213/aaedad](https://doi.org/10.3847/2041-8213/aaedad)
- Margalit, B., Metzger, B. D., & Sironi, L. 2020, MNRAS, 494, 4627, doi: [10.1093/mnras/staa1036](https://doi.org/10.1093/mnras/staa1036)
- McConnell, N. J., & Ma, C.-P. 2013, ApJ, 764, 184, doi: [10.1088/0004-637X/764/2/184](https://doi.org/10.1088/0004-637X/764/2/184)
- Merloni, A., Heinz, S., & di Matteo, T. 2003, MNRAS, 345, 1057, doi: [10.1046/j.1365-2966.2003.07017.x](https://doi.org/10.1046/j.1365-2966.2003.07017.x)
- Metzger, B. D., Margalit, B., & Sironi, L. 2019, MNRAS, 485, 4091, doi: [10.1093/mnras/stz700](https://doi.org/10.1093/mnras/stz700)
- Mezcua, M., Suh, H., & Civano, F. 2019, MNRAS, 488, 685, doi: [10.1093/mnras/stz1760](https://doi.org/10.1093/mnras/stz1760)
- Michilli, D., Seymour, A., Hessels, J. W. T., et al. 2018, Nature, 553, 182, doi: [10.1038/nature25149](https://doi.org/10.1038/nature25149)
- Molina, M., Reines, A. E., Greene, J. E., Darling, J., & Condon, J. J. 2021, ApJ, 910, 5, doi: [10.3847/1538-4357/abe120](https://doi.org/10.3847/1538-4357/abe120)
- Mooley, K. P., Margalit, B., Law, C. J., et al. 2021, arXiv e-prints, arXiv:2107.04703.
<https://arxiv.org/abs/2107.04703>
- Narayan, R. 1992, Philosophical Transactions of the Royal Society of London Series A, 341, 151, doi: [10.1098/rsta.1992.0090](https://doi.org/10.1098/rsta.1992.0090)
- Niu, C. H., Aggarwal, K., Li, D., et al. 2021, arXiv e-prints, arXiv:2110.07418. <https://arxiv.org/abs/2110.07418>
- Perley, D. A. 2019, PASP, 131, 084503, doi: [10.1088/1538-3873/ab215d](https://doi.org/10.1088/1538-3873/ab215d)
- Peterson, B. M. 1993, PASP, 105, 247, doi: [10.1086/133140](https://doi.org/10.1086/133140)
- Planck Collaboration, Aghanim, N., Akrami, Y., et al. 2020, A&A, 641, A6, doi: [10.1051/0004-6361/201833910](https://doi.org/10.1051/0004-6361/201833910)
- Reines, A. E., Condon, J. J., Darling, J., & Greene, J. E. 2020, ApJ, 888, 36, doi: [10.3847/1538-4357/ab4999](https://doi.org/10.3847/1538-4357/ab4999)
- Reines, A. E., Greene, J. E., & Geha, M. 2013, ApJ, 775, 116, doi: [10.1088/0004-637X/775/2/116](https://doi.org/10.1088/0004-637X/775/2/116)
- Reines, A. E., & Volonteri, M. 2015, ApJ, 813, 82, doi: [10.1088/0004-637X/813/2/82](https://doi.org/10.1088/0004-637X/813/2/82)
- Resmi, L., Vink, J., & Ishwara-Chandra, C. H. 2020, arXiv e-prints, arXiv:2010.14334.
<https://arxiv.org/abs/2010.14334>
- Rickett, B. J., Quirrenbach, A., Wegner, R., Krichbaum, T. P., & Witzel, A. 1995, A&A, 293, 479
- Romani, R. W., Narayan, R., & Blandford, R. 1986, MNRAS, 220, 19, doi: [10.1093/mnras/220.1.19](https://doi.org/10.1093/mnras/220.1.19)
- Rybicki, G. B., & Lightman, A. P. 1979, Radiative processes in astrophysics
- Sabater, J., Best, P. N., Hardcastle, M. J., et al. 2019, A&A, 622, A17, doi: [10.1051/0004-6361/201833883](https://doi.org/10.1051/0004-6361/201833883)
- Scholz, P., Spitler, L. G., Hessels, J. W. T., et al. 2016, ApJ, 833, 177, doi: [10.3847/1538-4357/833/2/177](https://doi.org/10.3847/1538-4357/833/2/177)
- Simard, D., & Ravi, V. 2021, arXiv e-prints, arXiv:2107.11334. <https://arxiv.org/abs/2107.11334>
- Slane, P. 2005, Advances in Space Research, 35, 1092, doi: [10.1016/j.asr.2005.04.029](https://doi.org/10.1016/j.asr.2005.04.029)
- Smail, I., Hogg, D. W., Yan, L., & Cohen, J. G. 1995, ApJL, 449, L105, doi: [10.1086/309647](https://doi.org/10.1086/309647)

- Spitler, L. G., Scholz, P., Hessels, J. W. T., et al. 2016, *Nature*, 531, 202, doi: [10.1038/nature17168](https://doi.org/10.1038/nature17168)
- Staelin, D. H., & Reifstein, Edward C., I. 1968, *Science*, 162, 1481, doi: [10.1126/science.162.3861.1481](https://doi.org/10.1126/science.162.3861.1481)
- Tachibana, Y., & Miller, A. A. 2018, *PASP*, 130, 128001, doi: [10.1088/1538-3873/aae3d9](https://doi.org/10.1088/1538-3873/aae3d9)
- Tendulkar, S. P., Bassa, C. G., Cordes, J. M., et al. 2017, *ApJL*, 834, L7, doi: [10.3847/2041-8213/834/2/L7](https://doi.org/10.3847/2041-8213/834/2/L7)
- The CHIME/FRB Collaboration, :, Amiri, M., et al. 2021, arXiv e-prints, arXiv:2106.04352. <https://arxiv.org/abs/2106.04352>
- Ulvestad, J. S. 2009, *AJ*, 138, 1529, doi: [10.1088/0004-6256/138/5/1529](https://doi.org/10.1088/0004-6256/138/5/1529)
- Varenius, E., Conway, J. E., Batejat, F., et al. 2019, *A&A*, 623, A173, doi: [10.1051/0004-6361/201730631](https://doi.org/10.1051/0004-6361/201730631)
- Vedantham, H. K., & Ravi, V. 2019, *MNRAS*, 485, L78, doi: [10.1093/mnrasl/slz038](https://doi.org/10.1093/mnrasl/slz038)
- Voggel, K. T., Seth, A. C., Baumgardt, H., et al. 2019, *ApJ*, 871, 159, doi: [10.3847/1538-4357/aaf735](https://doi.org/10.3847/1538-4357/aaf735)
- Walker, M. A. 1998, *MNRAS*, 294, 307, doi: [10.1046/j.1365-8711.1998.01238.x](https://doi.org/10.1046/j.1365-8711.1998.01238.x)
- Weisskopf, M. C., Hester, J. J., Tennant, A. F., et al. 2000, *ApJL*, 536, L81, doi: [10.1086/312733](https://doi.org/10.1086/312733)
- Wevers, T., van Velzen, S., Jonker, P. G., et al. 2017, *MNRAS*, 471, 1694, doi: [10.1093/mnras/stx1703](https://doi.org/10.1093/mnras/stx1703)
- Wevers, T., Stone, N. C., van Velzen, S., et al. 2019, *MNRAS*, 487, 4136, doi: [10.1093/mnras/stz1602](https://doi.org/10.1093/mnras/stz1602)
- Xiao, T., Barth, A. J., Greene, J. E., et al. 2011, *ApJ*, 739, 28, doi: [10.1088/0004-637X/739/1/28](https://doi.org/10.1088/0004-637X/739/1/28)